Journal of *Marine Science and Engineering*

MDPI

Article

Investigation of Edge Scour and Undermining Process of Conical Structure Around a Monopile

Jinming Tu [1,2,*], Fan Yang [1,2], Chi Yu [3] and Fuming Wang [1,2]

[1] School of Civil Engineering, Sun Yat-sen University, Guangzhou 510275, China; yangf356@mail.sysu.edu.cn (F.Y.)
[2] State Key Laboratory for Tunnel Engineering, Sun Yat-sen University, Zhuhai 519082, China
[3] Guangdong Energy Group Science and Technology Research Institute Co., Ltd., Guangzhou 511457, China
* Correspondence: tujm@mail2.sysu.edu.cn

Abstract

The scour protection performance of the conical structure under different slope angles, α, was investigated through numerical simulations. By solving the Navier–Stokes (N–S) equations, using the Renormalization Group (RNG) k–ε turbulence model and the Meyer-Peter and Müller (MPM) sediment transport formula, the scour protection performance, undermining process, and the flow field around the devices were fully analyzed at different slope angles. The findings indicate that the conical scour protection provides effective protection against scour damage. As the slope angle increases, greater scour depth is observed around the structure. A critical slope angle was identified between 30° and 40°, slope angle effects are obvious below the threshold; otherwise, it minimized. Undermining is the main cause of failure of such stiff scour protection, mainly driven by flow contraction and sand sliding. Upstream undermining beneath the structure is more pronounced, while the downstream undermining is largely related to the near-bed flow separation point. The critical undermining point (CUP) is proposed based on the undermining curve to distinguish the undermining state, which is critical in scour protection and structural stability.

Keywords: local scour; scour protection; undermining

1. Introduction

In recent years, with the large-scale development of offshore engineering, scour damage around pile foundations has become increasingly prominent. Scour is one of the failure reasons in marine structures. Scour holes reduce the bearing capacity of wind turbine foundations, increase the risk of structural failure, and severely threaten the in-situ stability of structure. Local scour will happen due to the combined action of upstream horseshoe vortex, wake vortex shedding, and streamline contraction, resulting in the formation and expansion of scour holes [1–7].

In response to the increasingly serious scour damage in offshore wind farms, numerous scholars have conducted research on scour protection methods. These methods can be generally categorized into active and passive protection, aiming at flow alternating and bed solidification, respectively [8]. The common active protection methods, such as the sacrificial piles, sills, artificial reefs, and slots on the pile, were investigated by many researchers [9,10]. Besides, some new flow-alternating devices, such as spoiler structures and artificial reefs, are also systematically studied. Scour protection performance largely depends on the shape and arrangements of the porous structure and shows good scour

Check for updates

Academic Editor: Constantine Michailides

Received: 30 November 2025
Revised: 29 December 2025
Accepted: 30 December 2025
Published: 2 January 2026

Copyright: © 2026 by the authors. Licensee MDPI, Basel, Switzerland. This article is an open access article distributed under the terms and conditions of the Creative Commons Attribution (CC BY) license.

protection performance [11–15]. Other bed solidification methods, such as collars, concrete mattresses, sediment grouting, and riprap, were also systematically studied [3,16–19]. Such bed solidification protection performance is highly affected by edge scour. For example, collar scour protection performance will be affected by its diameter, thickness, and elevation [17]. The scour hole will extend below the stiff collar, transforming from edge scour to undermining [20]. For stiff protection devices, the protection cannot follow the edge scour; it can be undermined by ongoing scour under the protection, and even lead to failure.

Lots of previous studies use the conical structures as scour depth reduction methods, which leads to upstream adverse pressure gradient reduction and ultimately decreases the horseshoe vortex strength. Some investigations have been conducted into the performance of the scour protection around conical structures. Sumer et al. [21] tested the shear stress distribution on the seabed around a rubble-mound breakwater and found that compared to upright cylindrical structures, the side slope significantly reduced the negative pressure gradient at the upstream side of the structure, thus the horseshoe vortex weakened significantly. Petersen et al. [18] conducted experiments using PIV methods to investigate the hydrodynamics and shear stress characteristics around the riprap protection. They found that reverse symmetric vortices occurred downstream due to conical-shaped riprap, resulting in significant scour holes downstream. The side slope angle has an obvious impact on the scour depth around conical piers. As the side slope angle decreases, the scour depth will be reduced accordingly, and the maximum scour depth will also be moved farther from the foundation edge [22,23]. And compared to collar protection aiming at downflow blockage, the slope of conical protection has a more pronounced impact on the three-dimensional flow field. To our knowledge, there is little research on scour protection performance of conical structures, and the slope angle effects are still unknown.

Besides, previous studies mostly focus on the scour depth development of the scour protection, and the scour hole extension has been seldom considered. However, the undermining is the primary factor influencing the performance of the bed solidification scour protection. The sediment under the protection could be washed away, and the protection performance could be significantly reduced [16,24,25]. The undermining also commonly happens around structures with shallow embedded foundations, such as the gravity base foundation, subsea caissons, spudcan foundation, and so on. And edge scour happens around the structure and then gradually extends under the foundation, which affects the stability of the structure. However, the undermining process has undergone limited research [26,27], and the mechanics of failing in scour protection caused by undermining is still unknown.

Herein, motivated by this phenomenon, the conical structure was used for scour protection around a monopile. This study provides a comprehensive three-dimensional numerical investigation into the scour protection performance and the undermining of conical protection structures. We specifically explore how the slope angle α influences the transition from edge scour to undermining. A new metric, the Critical Undermining Point (CUP), is introduced to define when scour holes from both sides merge beneath the foundation. The remainder of this paper is organized as follows: Section 2 details the numerical methodology and the 3D numerical model configuration. Section 3 presents a comparative analysis of flow characteristics and scour patterns under various slope angles. Finally, the key findings are summarized in Section 4.

2. Numerical Methodology

This section introduces the sediment condition and the governing equations for numerical simulation.

2.1. Numerical Simulation Setup

The sand used in the numerical simulation is uniform sand. The sand median particle size (d_{50}) is 0.486 mm, the relative density s (ratio of sand density to water density) is 2.65, and the repose angle φ is 32°. D is pile diameter of 0.2 m. To minimize the influence of the relative roughness of the sediment on local scour, it is assumed that when $D/d_{50} > 50$, its impact on local scour can be neglected [28]. The velocity was set to 0.35 m/s, and the sediment motion was controlled using the Shields number (θ, Shields Parameter). When the Shields number θ exceeds the critical Shields number (θ_{cr}), local scour occurs. The Shields number calculation is based on the improved formula proposed by Soulsby [29], as shown in Equations (1)–(5). The experiment was conducted in live-bed scour conditions, with $\theta/\theta_{cr} = 1.3$.

$$\theta_{cr} = \frac{0.30}{1 + 1.2D_*} + 0.055[1 - \exp(-0.020D_*)] \quad (1)$$

$$D_* = \left[g(s-1)/v^2\right]^{\frac{1}{3}} d_{50} \quad (2)$$

$$\theta = \frac{\tau_s}{\rho g(s-1)d_{50}} \quad (3)$$

$$\tau_s = \rho C_D \bar{U}^2 \quad (4)$$

$$C_D = [\kappa / ln(z_{os}/h) + 1]^2 \quad (5)$$

In the above equations, τ_s represents the shear stress, ρ is the fluid density, U is the flow velocity, and C_D is the drag coefficient. In Equation (5), κ denotes the von Kármán constant, with a value of 0.4. $\overline{U}$ refers to the depth-averaged flow velocity, and z_{0s} (calculated as $z_{0s} = d_{50}/12$) is the surface roughness. The sediment and flow properties are shown in Table 1.

Table 1. Velocity setting and sediment properties.

h/m	U/(m/s)	d_{50}/mm	D_*	θ	θ_{cr}	θ/θ_{cr}
0.5	0.35	0.486	11.88	0.041	0.031	1.3

To comprehensively investigate the influence of the structure's slope angle on the protection performance, six slope angles are considered, ranging from 10° to 50°, as shown in Table 2. The definition of the slope angle α is shown in Figure 1. When the structure slope angle varies, the protection extent remains constant at $3D$. Besides, to clearly illustrate the scour protection efficiency of the device, the scour reduction rate K_p was used to represent the effectiveness of the device in mitigating scour. Its definition is as follows:

$$K_p = \frac{S_0 - S_p}{S_0} \times 100\% \quad (6)$$

where S_0 is the scour depth without scour protection, S_p is the scour depth with scour protection.

Table 2. Test and numerical simulation conditions.

Test	Slope Angle α	Scour Depth S_p/D	K_p
B1	10	0.21	81%
B2	15	0.24	78%
B3	20	0.27	75%
B4	30	0.29	73%
B5	40	0.43	59%
B6	50	0.41	61%
B7	0	1.02	0

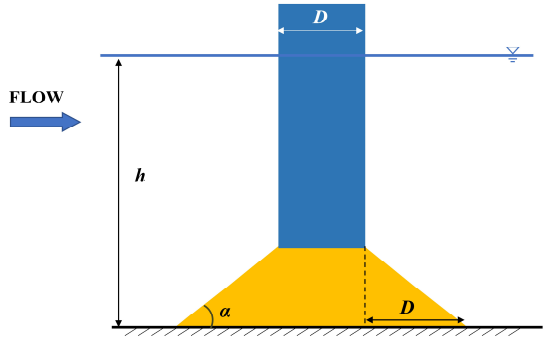

Figure 1. Sketch of the conical scour protection.

2.2. Governing Equations and Turbulence Model

The numerical simulation in this study is conducted through the Flow3D 2023R2 software, which solves the governing equations using the finite difference method. The software utilizes the FAVOR (Fractional Area Volume Obstacle Representation) technique and nested grid methods to effectively identify physical boundaries. The RNG k-ε model was applied, considering both the computational cost and accuracy. The governing equations for fluid flow are represented by the three-dimensional incompressible Reynolds-averaged Navier–Stokes (RANS) equations closed with the Re-normalization Group (RNG) k-ε turbulence model, expressed as Equations (7)–(9):

$$\nabla \cdot \vec{u} = 0 \tag{7}$$

$$\frac{\partial}{\partial x_i}(u_i A_i) = 0 \tag{8}$$

$$\frac{\partial u_i}{\partial t} + \frac{1}{V_F}\left(u_j A_j \frac{\partial u_i}{\partial x_j}\right) = -\frac{1}{\rho}\frac{\partial P}{\partial x_i} + f_i + g_i \tag{9}$$

where the $\vec{u}$ is velocity; A_i is the fractional area; x_i is the coordinate; u_i is the mean velocity components; f_i is viscous acceleration; g_i is gravity acceleration, the subscripts i = 1, 2, 3 represent the coordinate indices corresponding to the x, y, z directions, respectively. t is the time, p is fluid density; P is pressure, and V_F represents the fractional volume open to flow, and f_i can be calculated by:

$$f_i = \frac{1}{\rho V_F}\left[\frac{\partial}{\partial x_j}(A_j \tau_{ij})\right] \tag{10}$$

$$\tau_{ij} = \mu\left(\frac{\partial u_i}{\partial x_j} + \frac{\partial u_j}{\partial x_i}\right) - \frac{2}{3}\mu\delta_{ij}\frac{\partial u_k}{\partial x_k} \tag{11}$$

where the τ_{ij} is the shear stress (i, j = x, y, z) and can be calculated by Equation (11). δ_{ij} is the Kronecker delta.

Local scour often relates to high Reynolds numbers. Thus, the numerical simulation accuracy is significantly affected by the turbulence model. This study adopts the RNG model for scour simulation, which is more suitable for low turbulence intensity conditions compared to other models. Additionally, the RNG model can more accurately calculate wall shear stress, thereby improving the accuracy of sediment scour. The turbulence model has been used in many previous studies [30–34]. In the RNG turbulence model, the transport equation for turbulent kinetic energy k and the modeled equation for turbulent dissipation rate ε are depicted in Equation (12) and Equation (13), respectively:

$$\frac{\partial k_T}{\partial t} + \frac{1}{V_F}\left(uA_x\frac{\partial k}{\partial x} + vA_y\frac{\partial k}{\partial y} + wA_z\frac{\partial k}{\partial z}\right) = P_k + G_k + Diff_k - \varepsilon \tag{12}$$

$$\frac{\partial \varepsilon_r}{\partial t} + \frac{1}{V_F}\left(uA_x\frac{\partial \varepsilon}{\partial x} + vA_y\frac{\partial \varepsilon}{\partial y} + wA_z\frac{\partial \varepsilon}{\partial z}\right) = \frac{C_1\varepsilon}{k}\left(P_k + C_3G_k + Diff_\varepsilon - C_2\frac{\varepsilon^2}{k}\right) \quad (13)$$

where k is the specific kinetic energy, which is associated with turbulent velocity fluctuations; P_k denotes production of turbulent kinetic energy; G_k represents t the contribution of buoyancy to the generation of turbulent kinetic energy; ε is turbulent energy dissipation rate; $Diff_\varepsilon$ and $Diff_k$ are the diffusion terms; C_1, C_2 and C_3 are dimensionless parameters, in which C_1 and C_3 are constants of 1.42 and 0.2, respectively; and C_2 is computed from k and P_k in the RNG k-epsilon model [35].

2.3. Sediment Transport Model

Both suspended sediment transport and bedload transport are considered in the sediment transport model, which is commonly used in previous scour simulations [5–7]. The bedload transport formula significantly influences the scour development rate and the scour hole morphology. In this simulation, the Meyer-Peter and Müller bedload transport formula [36] is employed, as shown in Equations (14) and (15):

$$\Phi = \beta_{MPM}(\theta - \theta_{cr})^{1.5} \quad (14)$$

$$q_{b,s} = \Phi_s\left[g\left(\frac{\rho_s - \rho_w}{\rho_w}\right)d_s^3\right]^{0.5} \quad (15)$$

Here, Φ is the dimensionless sediment transport rate for bedload, which is related to the volumetric dimensionless bedload transport rate $q_{b,s}$. β_{MPM} is the bedload transport parameter, commonly at a value of 8.

In the sediment transport model, the diffusion of suspended sediment is achieved by solving its own transport equation, as shown in Equation (16).

$$\frac{\partial C_{s,i}}{\partial t} + \nabla\cdot(u_{s,i}C_{s,i}) = \nabla\cdot\nabla\left(D_fC_{s,i}\right) \quad (16)$$

where $C_{s,i}$ is the suspended sediment concentration, $u_{s,i}$ is the velocity of the suspended sediment, and C_f is the diffusion coefficient. Finally, bed surface changes are calculated by combining bedload and suspended sediment transport using the following Equation (17).

$$\frac{\partial z_b}{\partial t} + \frac{1}{(1-\varepsilon_b)}[q_b + E - F] = 0 \quad (17)$$

where z_b represents the bed surface elevation, E is the scour erosion rate, F is the deposition rate, ε_b is the seabed porosity

2.4. Computational Domain and Boundary Condition

Additionally, the incoming flow is fully developed through a long and empty flume ahead of the simulation, ensuring it conforms to the logarithmic velocity profile. Then, the fully developed flow was used in the scour simulation to reduce the computation cost, as depicted in Figures 2 and 3. Meanwhile, a certain length of fixed bed is reserved at both ends to ensure stable velocity profiles at the inlet and outlet boundaries and to prevent sediment from being washed away. The outlet boundary is pressure boundary, the bottom boundary is wall boundary, and the top and side boundaries are defined as symmetry boundaries, with zero normal velocity and all gradients in the normal direction being zero as well. The overall setup of the model is illustrated in Figure 3.

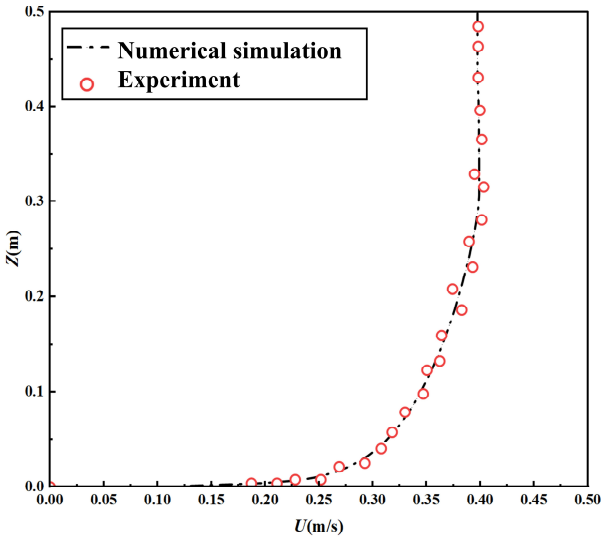

Figure 2. Velocity distribution along z axis.

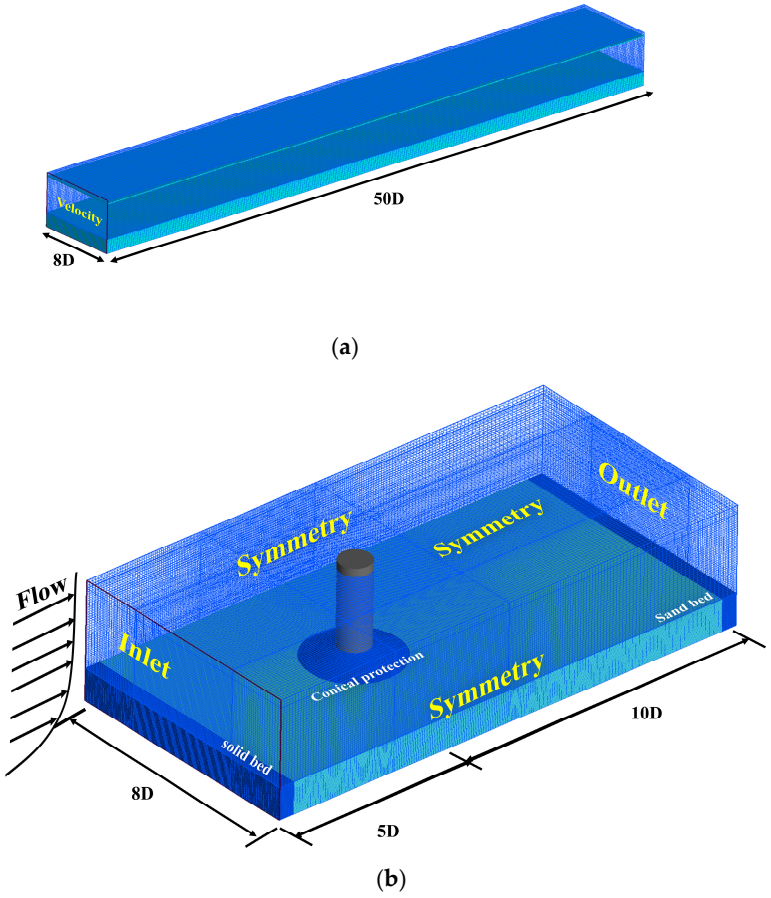

Figure 3. Numerical model setup and boundary conditions. (**a**) empty flume for velocity development; (**b**) numerical model for scour simulation.

The computational mesh size is essential to simulation accuracy. To guarantee both accuracy and efficiency of the simulations, the scour model has a width of 8D, 5D upstream from the inlet boundary, and 10D downstream from the outlet boundary, as shown in Figure 3b. A gradient-based mesh partitioning approach is employed with a mesh size of 1/25D around the structure. The mesh size gradually increases towards the edges of the model. The mesh size is also used in previous research [30,31,37]. The number of mesh

cells is approximately 2.4 million. The validation model has the same settings as the conical protection scour numerical model.

2.5. Validation of Numerical Model

The numerical simulation accuracy is validated in this chapter. Present numerical simulation results were validated against the experimental and numerical simulation results of Roulund et al. [38], as shown in Table 3. The accuracy of both the flow field and the scour development have been validated.

Table 3. Hydraulic and sediment parameters in the reference experiment.

	Scour Test	Rigid Bed Test
Water depth h (m)	0.4	0.54
Velocity U (m/s)	0.46	0.326
Boundary layer thickness δ (m)	0.2	0.54
Diameter D (m)	0.1	0.536
Seabed roughness k_s (mm)	0.55	0
Sand medium diameter d_{50} (mm)	0.26	
Shields number θ	0.55	

Before validating the model against the reference scour data, a mesh convergence analysis is carried out. Three mesh sizes, $0.10D$, $0.08D$, and $0.04D$, are used. The results are shown in Table 4 and Figure 4a. It can be observed that the medium mesh size shows good agreement with the reference numerical data, although some discrepancies still exist when compared with the experimental data. Therefore, the fine mesh size of $0.04D$ is adopted for the numerical simulations in this paper.

Table 4. Mesh convergence for validation.

	Coarse Mesh	Medium Mesh	Fine Mesh	Reference Exp.	Reference Num.
Mesh size	$0.1D$	$0.08D$	$0.04D$		
Scour depth (S_0/D)	0.93	1.09	1.21	1.05	1.23

The scour validation results are shown in Figure 4. It was found that the scour development reached an equilibrium state after 2000 s. The overall numerical simulation results show a good agreement with reference data. The maximum scour depth is located at the front of the pile. The maximum scour depth from the validation results closely matches with reference experimental data, but the scour depth in the downstream region is relatively little smaller. And the reference numerical data is relatively shallower compared to the experiment and validated simulation. This discrepancy may be attributed to the turbulence model: the RNG model is adopted in the present model, whereas the *k-ω SST* model was employed in the reference numerical model, and the suspended load process is not considered; thus, the downstream scour depth remains smaller. The simulated scour depth exhibits a 14% error relative to the reference values, yet it maintains an excellent agreement with the experimental results, with a difference of only 1%. Overall, the scour depth meets the requirements, and the accuracy of the model is convincing.

The hydrodynamics validation was conducted by comparing the distribution of the x-direction velocity with Roulund's [38] experimental results. Figure 5 shows the velocity distribution in the x-direction around the pile at different heights. It can be observed that the upstream velocity around the pile matches well with experimental data. However, as the height increases, discrepancies in velocity are observed in the downstream region of the pile. The present numerical data shows good agreement with the reference numerical

data, but they all show little discrepancies compared to the experimental data. And scour is determined by the near-bed velocity, thus the accuracy meets the requirements.

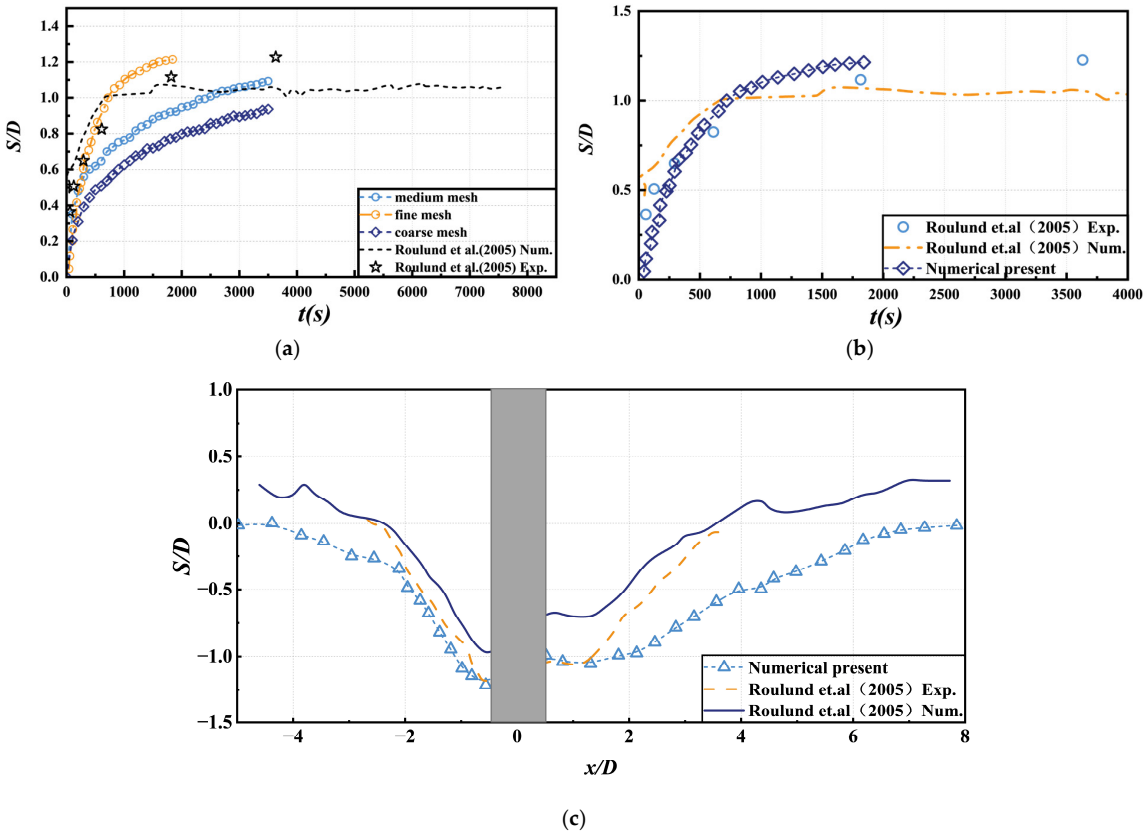

Figure 4. Validation results of Scour development around the monopile from Roulund et al. (2005) [38]. (**a**) mesh convergence results; (**b**) upstream scour depth of fine mesh; (**c**) longitude scour profile of fine mesh.

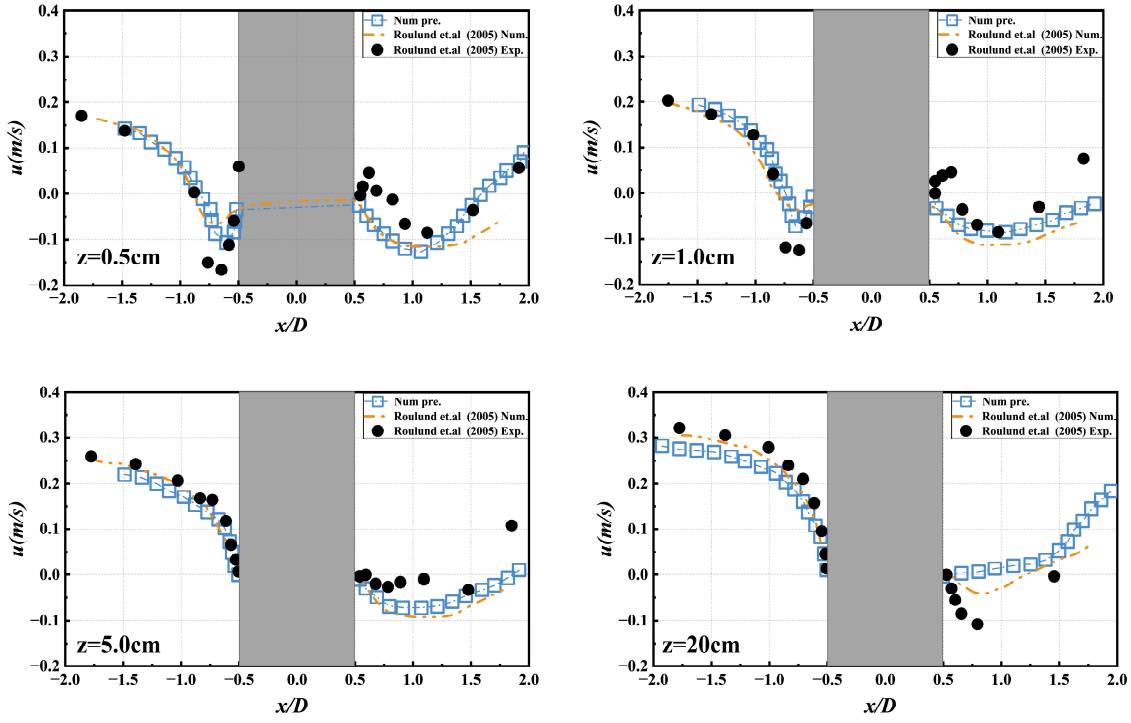

Figure 5. Horizontal velocity validation around the monopile from Roulund et al. (2005) [38].

3. Results and Discussion

3.1. Effects of Conical Structure on Scour Development

The scour topography is vital in local scour analysis. The effects of slope angle on scour protection performance are discussed in this chapter. It should be noted that since scour simulation is very computationally intensive, this study only simulates corresponding to a quasi-equilibrium state. And the equilibrium scour depth S_p depicted in Table 2 is calculated by Whitehouse's equation [4].

Figure 6 illustrates the scour development process around the pile under the protection of a conical structure at $\alpha = 30^\circ$ through numerical simulation. It can be observed that affected by the structure, a scour hole appears on both upstream and downstream sides of the pile, exhibiting notable differences compared to the scour hole around a single pile. The presence of the conical structure weakens horseshoe vortex intensity in front of the pile, resulting in reduced scour depth along the central axis of the structure. The maximum upstream scour depth appears on the edge of the structure, which is caused by velocity acceleration due to streamline contraction. In the downstream area, the scour holes are also evident, formed by accelerated velocity and streamline convergence, leading to approximately symmetric scour holes [18]. Different from the local scour around a monopile, due to the three-dimensional effects of the conical structure on the flow field, the streamline contraction in the downstream area is more obvious, accompanied by accelerated velocity downstream. This phenomenon will be further discussed in the next chapter. Under the influence of the wake flow field, sediment particles accumulate at the center, forming sand ridges. The whole scour map is similar to the scour pattern around cone-shaped riprap protection, reported by Petersen [18].

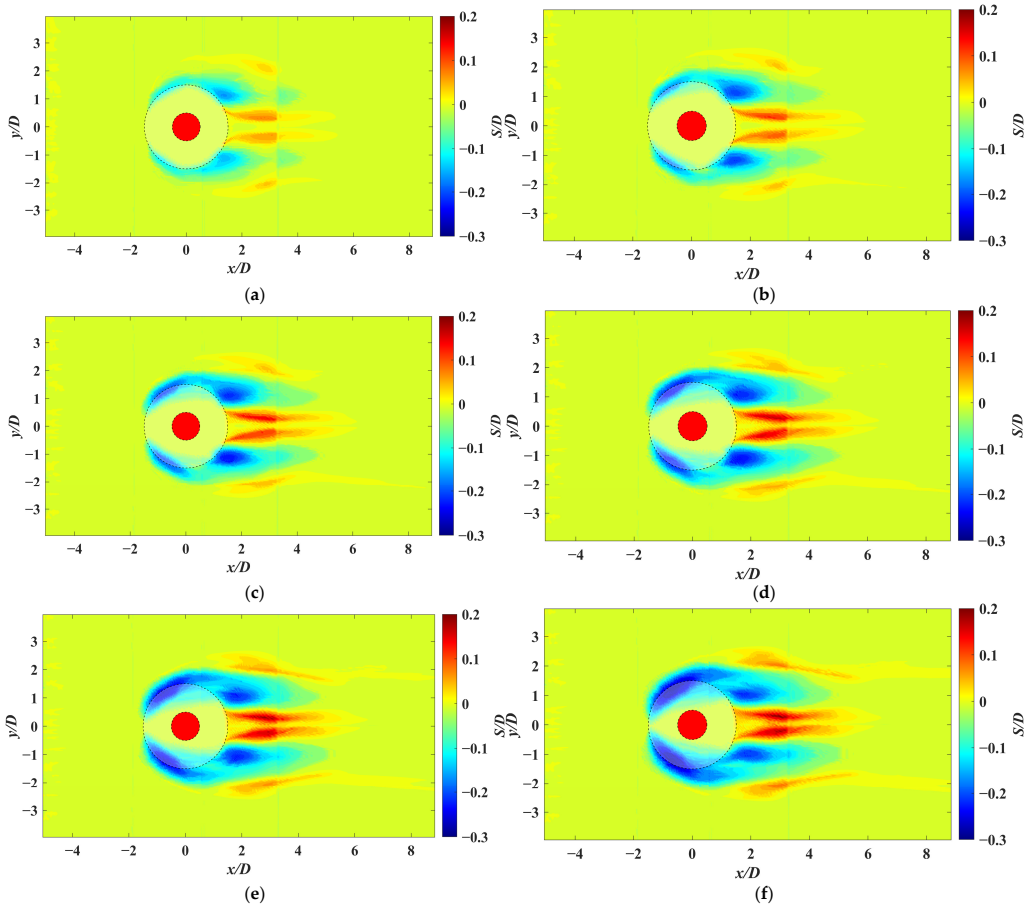

Figure 6. Scour profile evolution around the protective device at $\alpha = 30^\circ$. (**a**) t = 400 s; (**b**) t = 800 s; (**c**) t = 1200 s; (**d**) t = 1600 s; (**e**) t = 2000 s; (**f**) t = 2400 s.

Moreover, it is evident that the sediment scour rate around the conical structure varies significantly, as shown in Figure 7. During the initial phase of scour, due to the influence of downstream vortices and streamline contraction, the scour rate of the symmetric scour holes in the downstream region is relatively high, while the upstream scour rate is lower. As scour develops, upstream sediment is continuously transported further downstream, leading to a decrease in the scour rate of the downstream scour holes. Meanwhile, sediment beneath the upstream region of the structure gradually erodes, resulting in a higher development rate of scour in the upstream area.

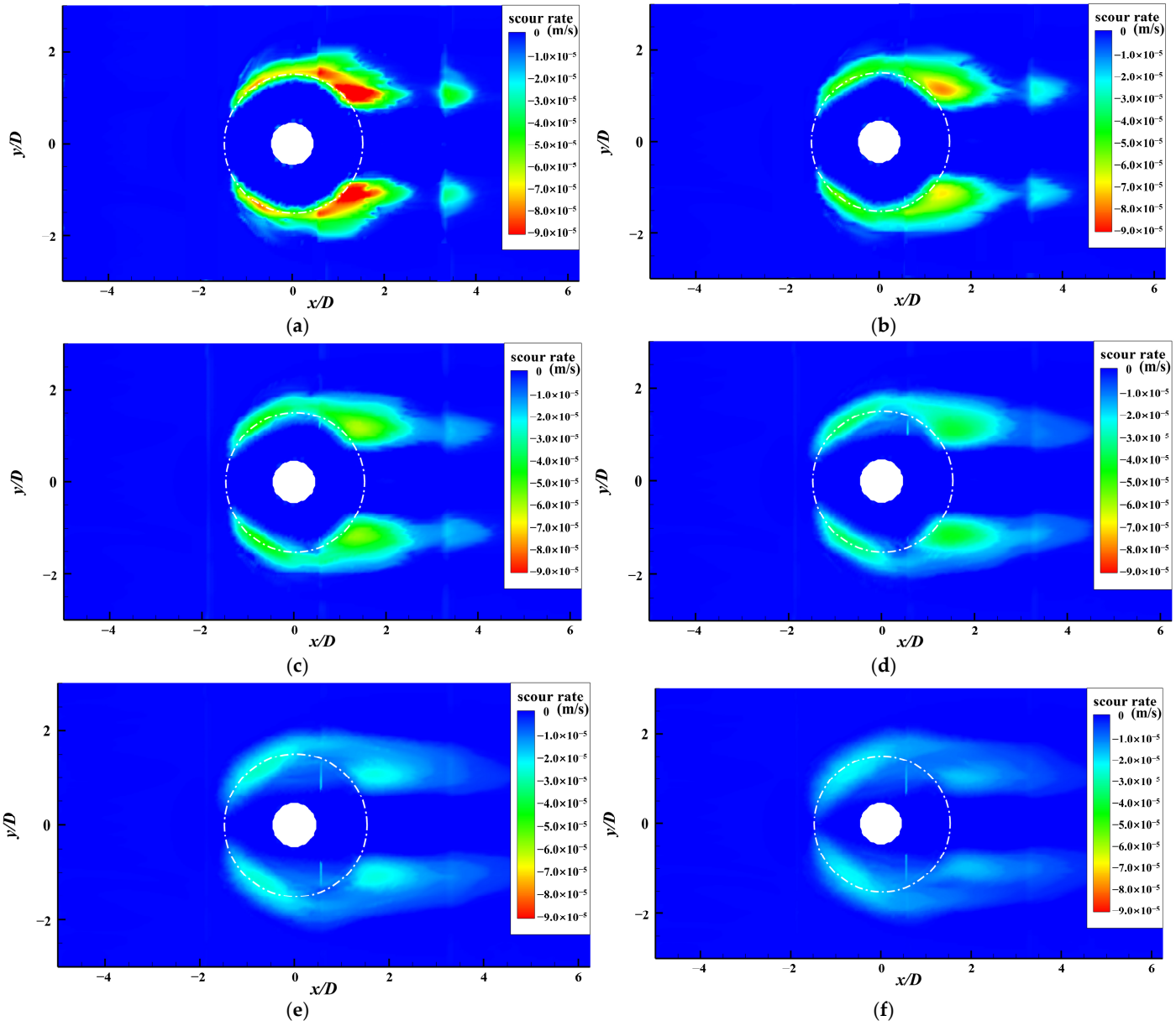

Figure 7. Sediment scour rate change in scour development at $\alpha = 30°$. (**a**) t = 200 s; (**b**) t = 400 s; (**c**) t = 600 s; (**d**) t = 1000 s; (**e**) t = 1800 s; (**f**) t = 2400 s.

Overall, the scour development process around the single pile with a conical structure can be divided into three stages. In the initial edge scour stage, the conical structure increases the blockage ratio, causing streamline contraction and an increase in bed shear stress. Sediment surrounding the structure is carried away, forming distinct edge scour, while deeper scour depths occur downstream under the influence of the wake flow. the conical structure is a rigid body, and it cannot follow the edge scour as it develops. Then it is

undermined by the ongoing edge scour. The second stage is the transition stage in the scour process as shown in Figure 6c,d, mainly from 800–1200 s. The scour depth and undermining both develop. However, the undermining area is relatively small while the scour depth develops rapidly. The third stage is dominated by undermining beneath the structure. During this stage, sediments continually slide down toward the bottom of the scour hole, where they are gradually carried away by water flow, further expanding the scour pit [18,39]. The undermining extension is more obvious as scour depth develops slowly.

3.2. Effetcs of Slope Angle α

3.2.1. Scour Depth Development

Based on the clarified scour characteristics under protection at slope angle $\alpha = 30°$, the protective effects of different structure slope angles ($\alpha = 10°, 20°, 30°, 40°, 50°$) is analyzed in the following paragraph. Figures 8 and 9 display the scour development and scour topography under different slope angles. It should be noted that the scour depth depicted in Figure 9 is extracted from the edge of the conical structure, which is mainly caused by undermining under the structure. The results indicate that as the slope angle increases, the scour depth at the edges of the structure increases, and the initial scour rate also rises. But in the cases of small slope angles (e.g., $\alpha = 10°, 15°$), the scour development shows almost similar patterns in the initial stage. And the difference could be observed after 1000 s, the increasing slope angle leads to a larger scour depth.

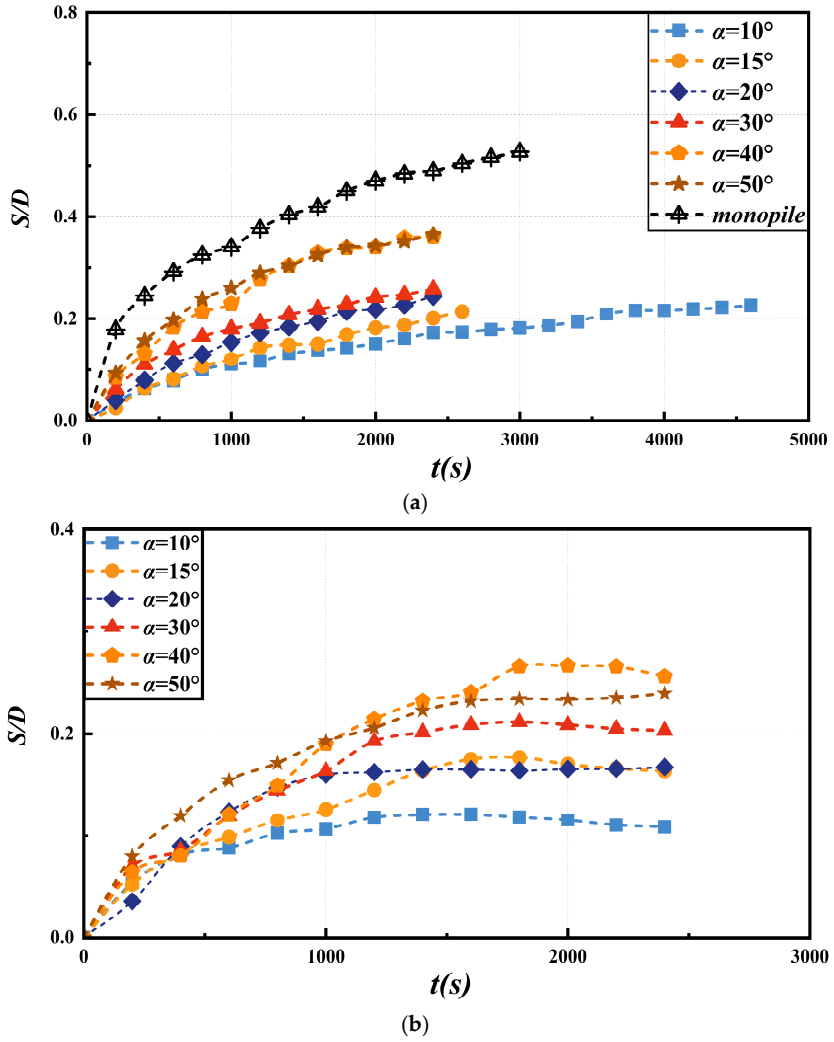

Figure 8. Scour development under different slope angles. (**a**) scour development under different slope angles. (**b**) Downstream scour development and backfilling process.

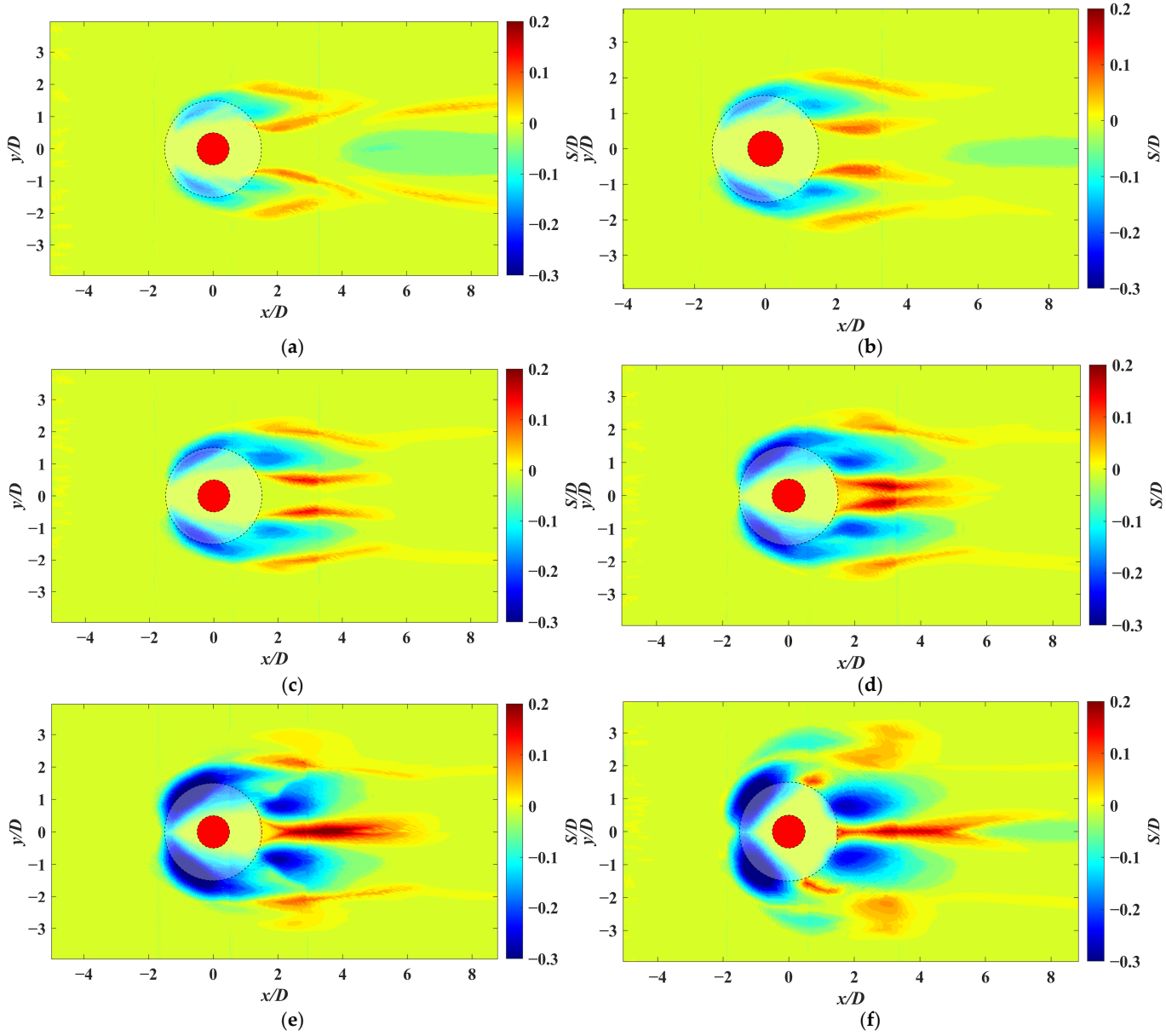

Figure 9. Scour topography under different slope angles. (**a**) α = 10°; (**b**) α = 15°; (**c**) α = 20°; (**d**) α = 30°; (**e**) α = 40°; (**f**) α = 50°.

Overall, within certain slope angle ranges, scour development exhibits similar patterns, specifically for $\alpha < 30°$, and $\alpha > 30°$. Within the two types, the edge scour development shows similar trends. When the slope angle is large, the scour depth has a boost when the slope angle increases from 30° to 40°. The initial scour rate is relatively higher when the slope angle increases to 40°. The effective diameter of the pile is large enough, resulting in similar sediment erosion patterns beneath the structure for α = 40° and 50°. And the scour depth boosts to $S/D > 0.35$, as the slope angle is above 30°, as illustrated in Figure 8a. The findings indicate a critical slope angle between 30° and 40°. Above this threshold, the scour depth is large but shows diminishing sensitivity to the slope angle α. Below this threshold, however, the variation in slope angle has a significant impact on the resulting scour depth.

Besides, the scour development of downstream scour holes exhibits a different pattern. Figure 8b illustrates the scour development process of the downstream scour hole. It can be clearly observed from the curve that the overall scour process is divided into two stages. The first stage is the scour development phase, which starts at 0 s and ends around 1500 s. This scour development in this stage is caused by the contraction of downstream

streamlines and the symmetric vortices, during which the scour depth gradually reaches a nearly equilibrium state. The second stage is the fluctuating phase. Fluctuations in scour depth result from the deposition of sediment transported by the incoming flow. It is widely acknowledged that scour development is a dynamically evolving process in which upstream sediment is continuously carried into the scour hole and then transported away by the flow. Due to the rapid development of the downstream scour hole during the initial stage, the overall trend shows an increase in scour depth. As the upstream scour hole continuously enlarges, sediment is carried into the downstream scour hole. Concurrently, the continuous expansion of the downstream scour hole leads to a reduction in flow velocity and turbulent energy. Consequently, the sediment-carrying capacity of the flow weakens, contributing to a decreasing trend in the observed scour depth.

The scour topographies under different slope angles are shown in Figure 9. Similarly, the scour hole extends from upstream to downstream. In the downstream region, sediment deposition is obvious on both sides of the scour hole; the sediment carried from the scour hole is deposited along them. And the scour hole region is similar at $\alpha \leq 30^\circ$, the upstream scour hole combined with the structure shows a circular curve. And when the slope angle is larger, the upstream scour hole obviously extends outward from the structure.

3.2.2. Undermining Process Around the Conical Structure

The undermining process beneath conical protection at different slope angles is shown in Figure 10. The lines in the figures exhibit the undermining area under the protection. Overall, the undermining process beneath the structure exhibits similar patterns.

Under smaller slope angles (e.g., $\alpha = 10^\circ$ and $\alpha = 15^\circ$), it is evident that the sediment undermining curves initially appear as an arc shape during the early stage, namely the edge scour. Subsequently, the undermining develops upstream and towards the centerline, evolving from its initial arc-shaped erosion range into a straight-line erosion range. During this stage, sediment undermining is driven by sediment sliding beneath the structure and flow velocity. Under the influence of the sediment repose angle, sediment continuously slides downward to the bottom of the scour hole and is transported by the water flow to the downstream region of the structure.

For larger slope angles (e.g., $\alpha = 40^\circ$ and $\alpha = 50^\circ$), the increase in slope angle leads to an increase in the blockage ratio. This results in intensified horseshoe vortex strength in front of the pile and flow velocity on the side of the structure, thus, more severe undermining beneath the structure. However, sediment erosion under large slope angles shows different characteristics compared to smaller angles. Unlike the straight-line undermining patterns that occur under small slope angles during equilibrium states, the undermining curves under large slope angles exhibit prominent V-shaped patterns in the flow direction. Moreover, the undermining develops more rapidly, and sediment is continuously eroded and transported downstream. In the downstream region ($0.5 < x/D < 1.0$), significant sediment accumulation is observed.

Herein, a critical undermining point (CUP) is proposed based on undermining curves, which means the two scour holes on both sides of the structure are combined into one large scour hole. The CUP marks the point where upstream sediment support is entirely removed, placing the structure at high risk of sinking and structural failure. It is also observed that as the slope angle increases, critical points appear earlier: at $\alpha = 40^\circ$, the critical erosion point emerges at t = 2000 s, whereas at $\alpha = 50^\circ$, it appears by t = 1200 s. It should be noted that for small slope angles, the CUP is not displayed in the erosion curves shown in the figure. However, this does not mean that it will not occur; as the scour hole expands, the CUP may or may not emerge during the final stages of the scouring process.

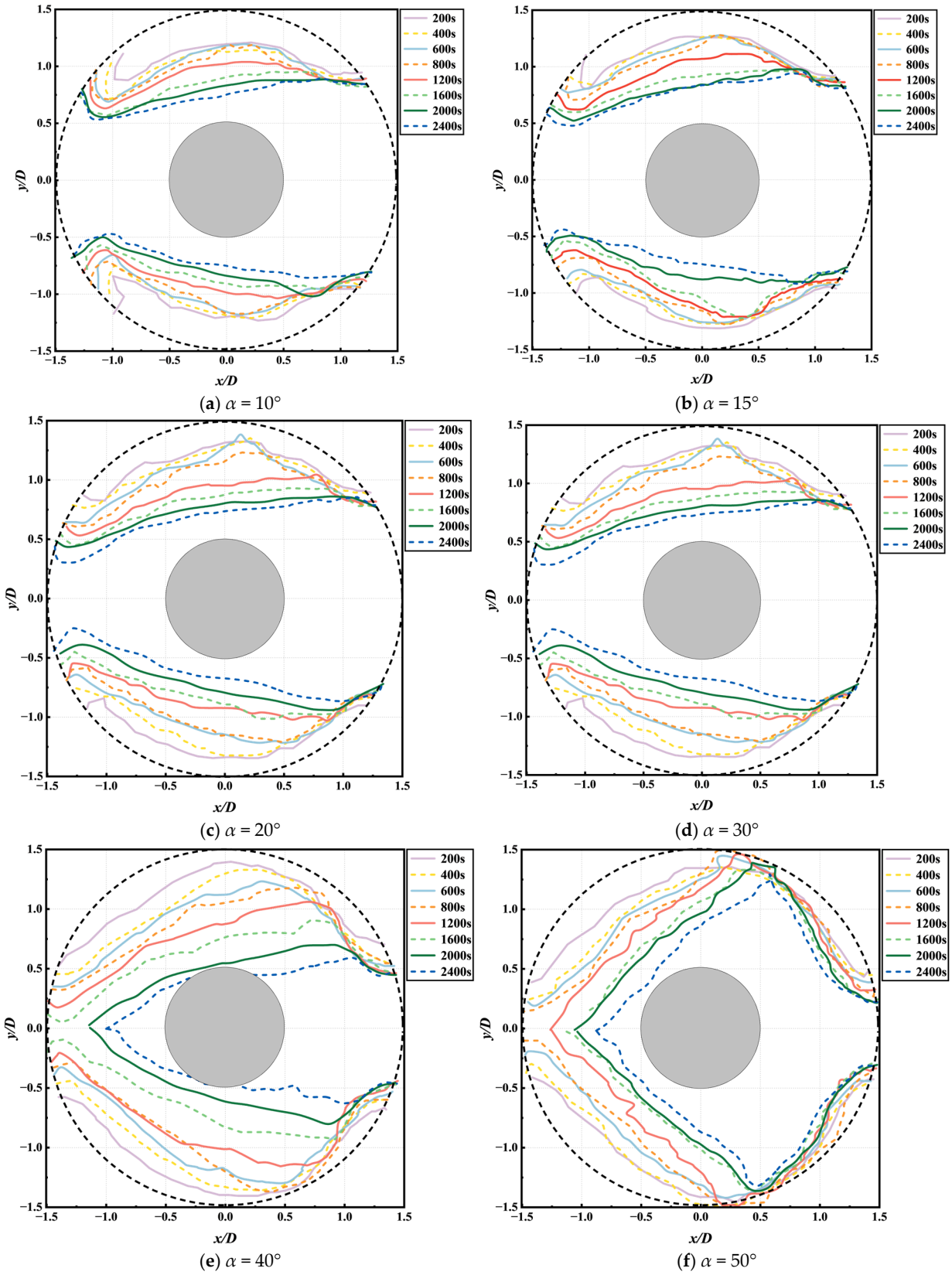

Figure 10. Undermining process under different slope angles. (**a**) α = 10°; (**b**) α = 15°; (**c**) α = 20°; (**d**) α = 30°; (**e**) α = 40°; (**f**) α = 50°.

At $\alpha = 40°$, in the upstream area ($x/D < 0$), the undermining curve gradually converges toward the pile as scour develops. However, in the downstream area ($x/D > 0$), the erosion curve at t = 800 s appears outside of that at t = 600 s, indicating sediment accumulation.

Subsequently, between t = 800 s and t = 2400 s, the erosion range in the downstream region ($0 < x/D < 1.0$) progressively converges toward the pile, while the undermining curves in the $x/D > 1.0$ range show relatively minor changes as scour develops. And this phenomenon can be explained by the flow field.

At $\alpha = 50°$, scour undermining development is even more rapid. The critical erosion point emerges at t = 1200 s. It is also observed that due to the rapid expansion of the upstream scour hole, undermining curves appear outside the structure in the range of $0 < x/D < 0.5$, indicating significant sediment deposition as shown in scour topography, displayed in Figure 10f. A significant sediment accumulation on both sides of the structure. Thus, a distinct low velocity area is observed , which is the reason for a tiny undermining downstream of the structure. Figures in Section 3.3 show that there are two main velocity peaks in the near-bed averaged velocity at $\alpha = 40°$ and $\alpha = 50°$. One appears on both sides of the conical structure, and another one is downstream of the conical structure. The location of the upstream peak velocity corresponds to the scour area, which is the reason for undermining under the structure. Also, a relatively lower velocity area can also be observed downstream of the peak velocity area, which indicates a slow scour development for a range of $0 < x/D < 1.0$.

3.2.3. Seabed Shear Stress Distribution

The Shields number θ is the predominant parameter for sediment transport, which is controlled by shear stress. And this shear stress distribution is discussed in this chapter, as shown in Figure 11. Figure 11a depicts the separation distance of the horseshoe vortex, and Figure 11b shows the shear stress amplification factor along Y = 0 on the bed surface.

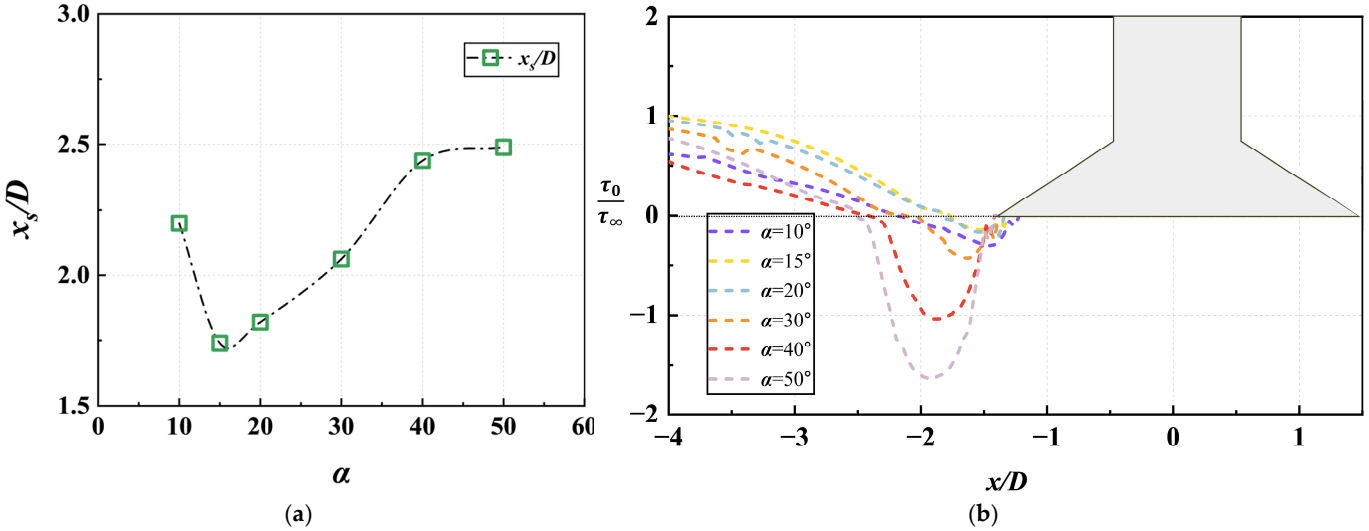

Figure 11. Shear stress distribution under different slope angles. (**a**) horseshoe vortex separation distance; (**b**) shear stress amplification factor along Y = 0.

It can be observed that, as the slope angle increases, the separation point distance (x_s) of the horseshoe vortex on the bed surface gradually increases, and the size of the horseshoe vortex also rises. The location of the maximum shear stress in the upstream region coincides with the horseshoe vortex. However, when the slope angle α exceeds 40°, the separation point of the horseshoe vortex shows negligible variation despite the increase in slope angle. The reason is that the larger slope angle has little effect on the structure's effective diameter, so the horseshoe vortex changes only slightly.

Meanwhile, the shear stress amplification factor τ/τ_{cr} at $\alpha = 50°$ is above 1, the initial scour did not start from upstream according to undermining curve in Figure 10. This

indicates that, under the effect of the conical structure, upstream scour hole is not directly initiated by the horseshoe vortex, while the edge scour caused by flow contraction and sand sliding mainly contributes to undermining process, which becomes the primary driver for scour holes expansion.

3.3. Flow Characteristics

3.3.1. Downstream Vortices Distribution

To further clarify the influence of the conical structure on the overall flow field, Figure 12 depicts the flow characteristics downstream of the conical structure at $\alpha = 30°$. Velocity field slices along the Y–Z plane were extracted at positions $x/D = 1.5$, $x/D = 2$, $x/D = 2.5$, and $x/D = 3$. The results show that the conical structure affects the interaction of the shear layer on the sides of the cylinder, leading to a significant multi-vortex flow field in the wake region.

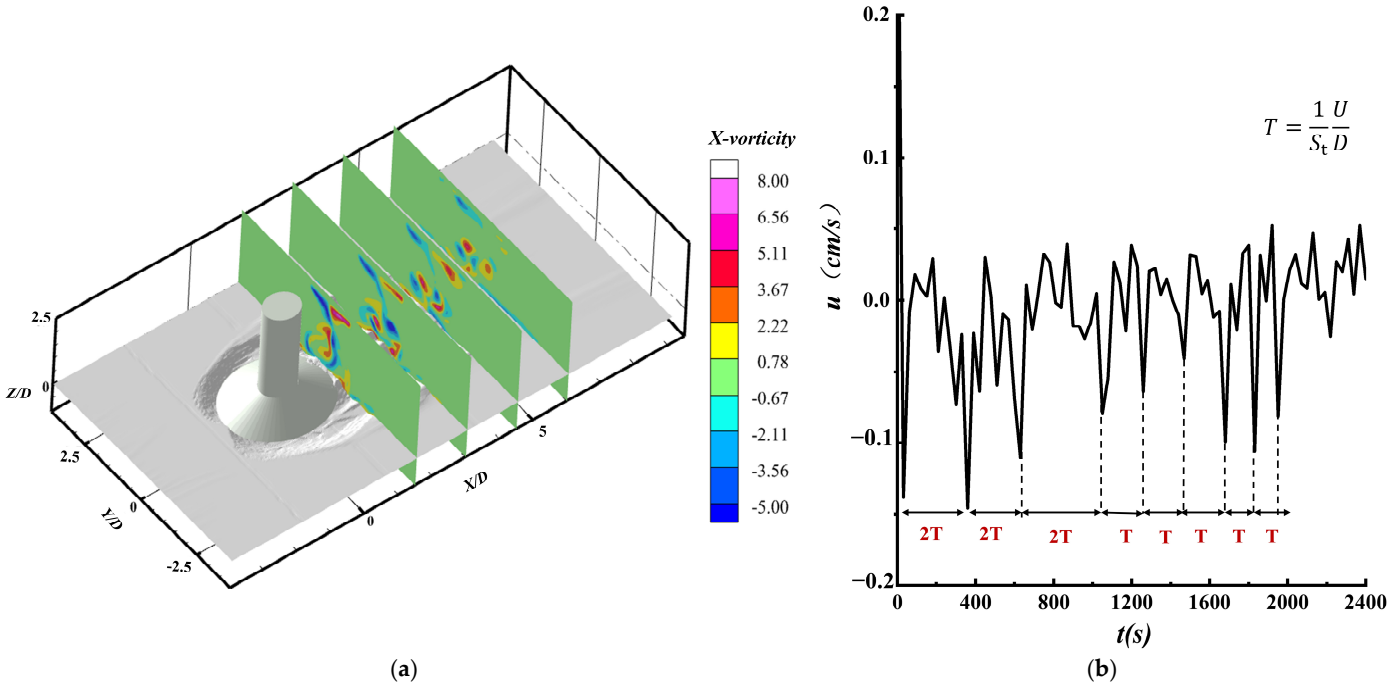

(**a**) (**b**)

Figure 12. Downstream vorticity distribution at $\alpha = 30°$. (**a**) downstream vortices; (**b**) downstream streamwise velocity.

The red areas in Figure 12 represent clockwise rotating vortices, while the blue areas represent counterclockwise rotating vortices. It can be observed that, due to the influence of the conical structure, a nearly symmetrical twin-vortex structure appears downstream. This vortex system resulted from the wake region of the pile and the conical structure. The shear layers interact to form the wake vortexes; however, due to the different diameters and shapes of the two structures, the wake vortex seems to be separated for the two structures when $\alpha = 30°$. Besides, the magnitude of velocity is small near the bed; thus, the vortex supply is smaller than the outer region. As a result, the vortex shedding slows down at the bottom, and the twin-vortex structure is observed in the vertical direction of the flow. Furthermore, because of the roughness of the sediment bed, small-scale vortices are present near the bed surface. These vortices are generated by the convergence of water flow near the bed surface. To further clarify the characteristics of the downstream flow field, the x velocity at $x/D = 1.5$, $y/D = 0.5$ is shown in Figure 12b. The fluctuation period T of the flow velocity is defined as:

$$T = \frac{1}{S_t}\frac{D}{U} \tag{18}$$

The Strouhal number (S_t) represents the normalized vortex shedding frequency. It can be observed that the flow velocity along the x-axis at this position is negative, and the velocity exhibits quasi-periodic fluctuations. At this location, most velocity peaks are negative due to vortex shedding, with only a few positive peaks. The dominant negative peaks are consistent with the findings of Baykal [40], where vortex shedding frequencies near the bed surface exhibited two peaks. The intervals of certain velocity peaks correspond to a period T, while other intervals correspond to 2T, which is attributed to the twin-vortex structure. Since the observation point is located between the near-bed flow region and the outer flow region, the flow variations exhibit two distinct periods, similar to the results of Petersen et al. [18].

3.3.2. Time-Averaged Near-Bed Velocity

Bed shear stress is a key parameter in sediment transport and depends on near-bed velocity. Figure 13 shows the time-averaged velocity in the equilibrium stage near the bed surface ($z/D = 0.007$). Of worth noting that the flow velocity near the centerline downstream of the structure is very low, because this area is the sediment deposition region, resulting in a very low time-averaged velocity, especially when the slope angle is large, where the velocity is almost zero.

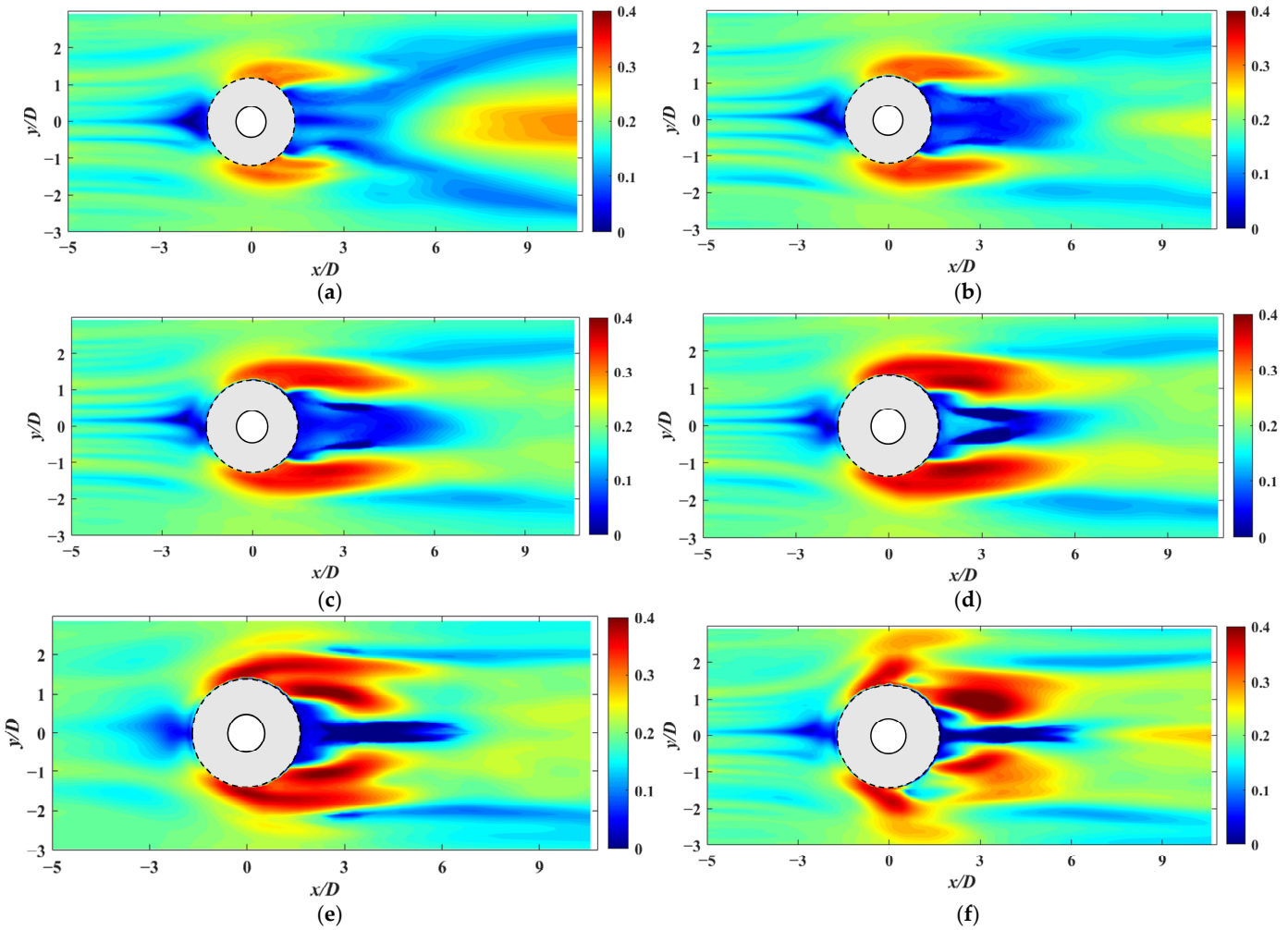

Figure 13. Time-averaged velocity at different slope angles. (**a**) α = 10°; (**b**) α = 15°; (**c**) α = 20°; (**d**) α = 30°; (**e**) α = 40°; (**f**) α = 50°.

From the time-averaged velocity field, it can be observed that as the slope angle increases, the streamline contraction on both sides of the structure intensifies, and the

velocity on both sides of the structure increases. And it is evident that there are two velocity peaks in the streamline contraction area. One is on the side of the structure, approximately located at $x/D = 0$; the other peak is located downstream of the structure, corresponding to the symmetry downstream scour hole. The upstream velocity peak is attributed to the blockage effects; the maximum velocity always appears on both sides of the structure when the flow passes around the structure. However, the reason for the downstream velocity peak seems more complex. Different from the flow around cylindrical structures, the accelerated velocity region of the conical structure is wider downstream, and the downstream velocity is higher due to the three-dimensional effects of the conical structure. Thus, the symmetry scour hole is formed due to increased velocity.

Besides, it should be noted that the downstream scour hole is caused by increased velocity. Thus, the downstream scour hole is larger and deeper in the initial development stage. An obvious shallower area of the scour region can be seen between the two scour holes, as shown in Figures 6 and 9. Thus, the undermining area of $0 < x/D < 1$ under the structure is less severe, and sediment accumulation even appears at $\alpha = 50°$. The near-bed velocity field could be divided into two parts: $x/D < 1$ and $x/D > 1$. The regions of accelerated and decelerated flow velocity around the structure, demarcated by the flow separation point approximately at $x/D = 1$, regardless of the slope angle. This phenomenon, reflected in the undermining curve, shows that the undermining area of $x/D > 1$ does not change significantly.

3.3.3. Turbulence Kinetic Energy Distribution

Also, local scour is not only affected by the near-bed velocity, but also by the vertical velocity. The three-dimensional streamline will affect the energy transport and downstream sediment deposition [41]. Figure 14 illustrates the distribution of turbulence kinetic energy (TKE) along the $y/D = 0$ profile under different slope angles. TKE can be used to analyze the primary vortex structures and energy transfer mechanisms within the time-averaged flow field, and the definition is:

$$TKE = \frac{1}{2}\left(u'^2 + w'^2\right) \tag{19}$$

where the u' and w' represent the fluctuating velocity in x and z directions. It can be observed that two distinct TKE peaks appear in the wake region at small slope angles ($\alpha = 10$–$15°$). In such circumstances, the wake vortices generated by conical protection and the pile are relatively independent. As a result, two relatively isolated TKE peaks appear downstream of the structure at lower angles. One of the peak areas is located at $x/D = 2.5$, which depends on the diameter of the conical structure. And the peak area is close to the conical structure. As the slope angle increases to $\alpha = 20°$, the exposed height of the structure increases, and the downstream wake gradually transitions to a single-peak area, and the peaks' location is still at $x/D = 2.5$.

As the slope angle increases to a larger value ($\alpha = 30$–$50°$), the obvious finding is the peak and trough areas of the TKE. These energy variations in the vertical direction suggest complex interactions between the wake vortices of the conical structure and the flow disturbances from the single pile. Additionally, the TKE distribution of the large slope angle condition shows a totally different pattern: The peak TKE area moves upwards due to the influence of the conical structure. The low energy area is observed near the bed surface, which is caused by the shelter effects of the conical structure. Thus, the sand accumulation is observed in the scour topography.

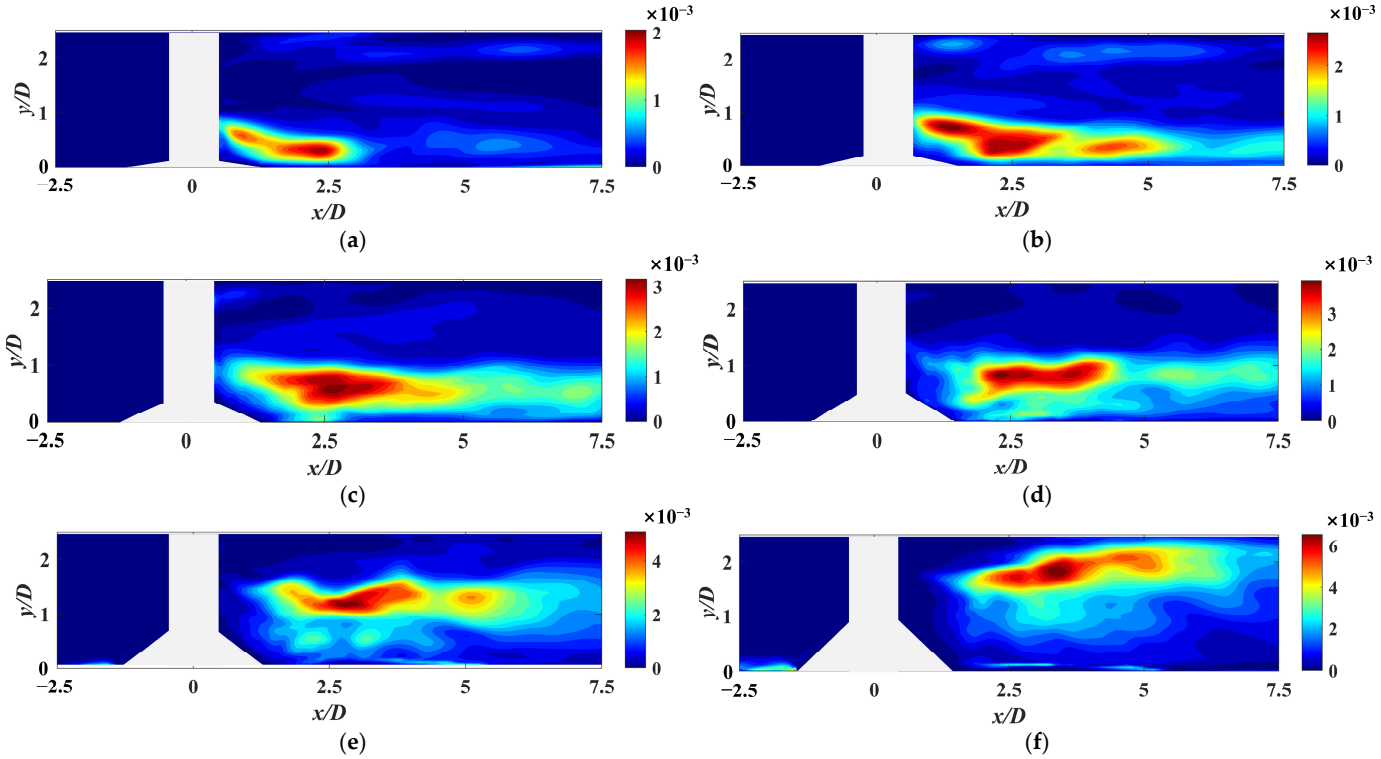

Figure 14. Turbulent kinetic energy distribution under different side slope angles α. (**a**) α = 10°; (**b**) α = 15°; (**c**) α = 20°; (**d**) α = 30°; (**e**) α = 40°; (**f**) α = 50°.

Incoming flow can be separated into two parts when it encounters the conical protection: upper flow above the conical structure and bottom flow in the scour hole. To fully present the velocity change in the scour hole, Figure 15 displays the velocity change in the scour hole as the scour hole develops and the suspended sediment concentration at y/D = −0.2, where the scour hole develops both upstream and downstream. The suspended sediment concentration, to some extent, represents the development rate of scour: a higher suspended sediment concentration indicates a higher scour development rate. Overall, the scour development beneath the structure does not exhibit a strictly linear relationship with the local flow velocity beneath it (i.e., a higher velocity does not necessarily correspond to a higher suspended sediment concentration).

At the initial stage, under the influence of streamline contraction, sediment is mobilized, and scour initiates and develops. After the scour hole forms, the flow velocity at the bottom of the scour hole is amplified due to flow blockage by the structure, and sediment at the scour-hole bottom is transported away. However, the flow velocity directly beneath the structure decreases significantly, while the corresponding suspended sediment concentration remains relatively high, indicating a lateral expansion of the scour hole. This lateral expansion is mainly governed by the sediment repose angle, whereby the upper sediment continually slides down into the bottom of the scour hole.

When the scour hole has developed to a certain extent (approximately 600–1000 s), its size increases, and the velocity difference between the upstream and the underside of the structure becomes pronounced under the action of the incoming flow, leading to significant flow separation. During this stage, the scour hole continues to grow as a whole and expands laterally.

After the upstream scour hole and downstream scour hole are fully connected beneath it (approximately 1000–2400 s), flow separation and bypass around the conical structure become prominent. Once the upstream and downstream scour holes are connected, the local increase in flow velocity beneath the structure caused by streamline contraction

becomes the dominant factor driving the undermining beneath the structure. In this stage, the scour hole exhibits marked lateral expansion, while the variation in scour depth is relatively small.

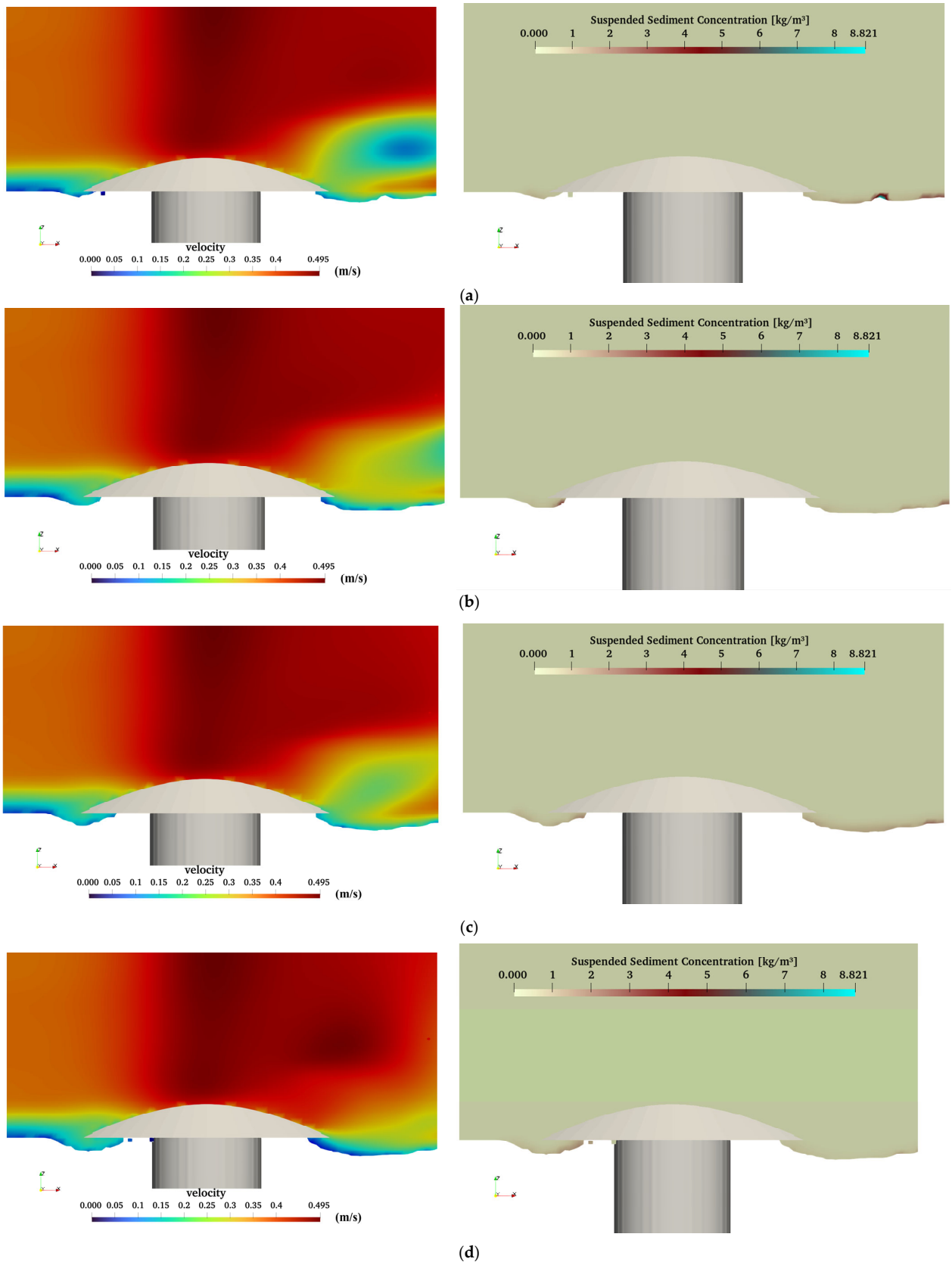

Figure 15. *Cont.*

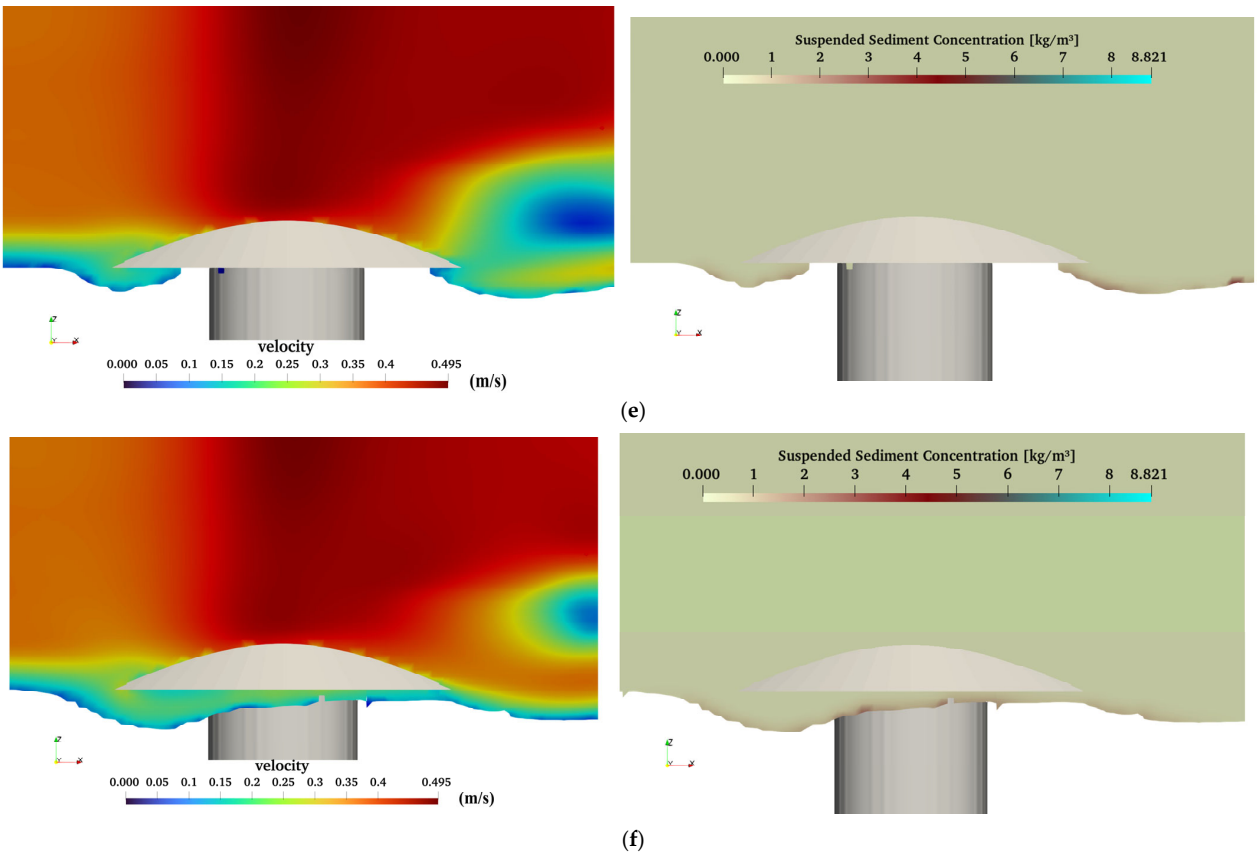

Figure 15. Flow field around the conical structure at y/D = 1. (**a**) t = 200 s; (**b**) t = 400 s; (**c**) t = 600 s; (**d**) t = 800 s; (**e**) t = 1000 s; (**f**) t = 2400 s.

4. Conclusions

Through numerical simulations, the local scour and undermining process of a conical scour protection around a monopile is investigated. The slope angle effects on scour protection performance, undermining process, and hydrodynamics are fully analyzed. The main conclusions of the study are as follows:

1. Conical structures exhibit excellent scour protection performance. Compared with unprotected conditions, their scour protection efficiency can exceed 70%. Furthermore, the protective performance improves as the slope angle decreases. A critical slope angle was identified between 30° and 40°. The slope angle exerts a pronounced influence on scour depth below this range, whereas its effect diminishes significantly at higher angles.
2. The undermining process is also affected by slope angle α. Local scour around conical scour protection could be divided into two main stages: the initial edge scour stage and the undermining stage. Upstream undermining is obvious, while the downstream undermining is not significant due to flow separation and shield effects. Downstream undermining development is largely related to the flow separation point of near-bed velocity. The critical undermining point (CUP) is proposed based on the undermining curve, which means the two side edge scours hole develops to be combined into one. The CUP distinguishes between different states of undermining, and it is vital for structural stability. When the slope angle α is large, the CUP appears; otherwise, it does not appear or appears in a later scour stage.
3. Two symmetry vortices were observed downstream. The downstream undermining area is related to near-bed flow separation. Also, the turbulent kinetic energy peaks vary with increasing slope angle. The maximum value is located around x/D = 2.5,

and the peak position of turbulent kinetic energy shifts upward as the slope angle increases.

In summary, these findings provide practical guidelines for optimizing protection geometry considering long-term structural stability. While the RNG k-ε model proved effective in this study, it may not resolve the finest turbulent structures as precisely as LES or DNS models. Future research should utilize high-fidelity models to further enhance predictive accuracy. Furthermore, subsequent studies should address wave-current interactions and scale effects to ensure the applicability of these results to full-scale offshore engineering projects.

Author Contributions: Methodology, J.T.; Software, J.T.; Validation, J.T.; Formal analysis, F.Y. and C.Y.; Resources, C.Y.; Writing—original draft, J.T.; Writing—review & editing, F.Y.; Supervision, C.Y. and F.W.; Project administration, F.W.; Funding acquisition, F.Y., C.Y. and F.W. All authors have read and agreed to the published version of the manuscript.

Funding: This work was supported by the Marine Economic Development Program of Guangdong province, China (Grant No. 29 [2023]).

Data Availability Statement: The raw data supporting the conclusions of this article will be made available by the authors on request.

Conflicts of Interest: Author Chi Yu is employed by the company Guangdong Energy Group Science and Technology Research Institute Co., Ltd. The remaining authors declare that the research was conducted in the absence of any commercial or financial relationships that could be construed as potential conflicts of interest.

References

1. Gazi, A.H.; Afzal, M.S. A review on hydrodynamics of horseshoe vortex at a vertical cylinder mounted on a flat bed and its implication to scour at a cylinder. *Acta Geophys.* **2020**, *68*, 861–875. [CrossRef]
2. Guan, D.-W.; Xie, Y.-X.; Yao, Z.-S.; Chiew, Y.-M.; Zhang, J.-S.; Zheng, J.-S. Local scour at offshore windfarm monopile foundations: A review. *Water Sci. Eng.* **2021**, *15*, 29–39. [CrossRef]
3. Tang, Z.-H.; Melville, B.; Singhal, N.; Shamseldin, A.; Zheng, J.-H.; Guan, D.-W.; Cheng, L. Countermeasures for local scour at offshore wind turbine monopile foundations: A review. *Water Sci. Eng.* **2022**, *15*, 15–28. [CrossRef]
4. Mutlu, S.B.; Jørgen, F. *The Mechanics of Scour in the Marine Environment*; World Scientific: Singapore, 2002.
5. Hu, D.; Tang, W.; Sun, L.; Li, F.; Ji, X.; Duan, Z. Numerical simulation of local scour around two pipelines in tandem using CFD–DEM method. *Appl. Ocean Res.* **2019**, *93*, 101968. [CrossRef]
6. Hu, Z.; Li, Y.P. Full-scale tsunami-induced scour around a circular pile with three-dimensional seepage. *Coast. Eng.* **2025**, *197*, 104676. [CrossRef]
7. Hu, Z.; Qi, W.-G.; Li, Y.P. The Role of Dynamic Seepage Response in Sediment Transport and Tsunami-Induced Scour. *J. Geophys. Res. Ocean* **2025**, *130*, e2024JC021084. [CrossRef]
8. Chiew, Y.M. Scour Protection at Bridge Piers. *J. Hydraul. Eng.* **1992**, *118*, 1260–1269. [CrossRef]
9. Kumar, V.; Raju Kittur, G.R.; Vittal, N. Reduction of Local Scour around Bridge Piers Using Slots and Collars. *J. Hydraul. Eng.* **1999**, *125*, 1302–1305. [CrossRef]
10. Chiew, Y.; Lim, S. Protection of bridge piers using a sacrificial sill. *Proc. Inst. Civ. Eng. Water Marit. Eng.* **2003**, *156*, 53–62. [CrossRef]
11. Zhai, Y.; Fuhrman, D.R.; Damgaard Christensen, E. Numerical simulations of flow inside a stone protection layer with a modified k-ω turbulence model. *Coast. Eng.* **2024**, *189*, 104469. [CrossRef]
12. Ismail, H.; Xu, Y.; Liu, X. Flow and scour around idealized porous engineered log jam structures. *J. Hydraul. Eng.* **2021**, *147*, 04020089. [CrossRef]
13. Fan, Y.; Lili, Q.; Guoqiang, T.; Lin, L. Local scour around a porous surface-piercing square monopile in steady current. *Ocean Eng.* **2021**, *223*, 108716. [CrossRef]
14. Qi, H.; Wang, J.; Zou, W.; Luo, W.; Tian, W.; Li, J. Characteristics and mechanism of local scour reduction around spur dike using the collar in clear water. *Sci. Rep.* **2024**, *14*, 12299. [CrossRef]

15. Liu, X.; Chen, J.; Lei, Y.; Liu, R.; Zhou, Y.; Li, H.; Yuan, J. An experimental study of using artificial reefs as scour protection around an offshore wind monopile. *Ocean Eng.* **2025**, *337*, 121932. [CrossRef]
16. Tang, Z.; Melville, B.; Shamseldin, A.Y.; Singhal, N.; Guan, D. Experimental study of bed solidification as a local scour countermeasure for offshore wind turbine monopile foundations. *Ocean Eng.* **2024**, *299*, 117369. [CrossRef]
17. Tang, Z.; Melville, B.; Shamseldin, A.; Guan, D.; Singhal, N.; Yao, Z. Experimental study of collar protection for local scour reduction around offshore wind turbine monopile foundations. *Coast. Eng.* **2023**, *183*, 104324. [CrossRef]
18. Petersen, T.U.; Mutlu Sumer, B.; Fredsøe, J.; Raaijmakers, T.C.; Schouten, J.-J. Edge scour at scour protections around piles in the marine environment—Laboratory and field investigation. *Coast. Eng.* **2015**, *106*, 42–72. [CrossRef]
19. Shahhosseini, M.; Yue, S.; Xu, J.; Zhang, M.; Yu, G. Scour depth at a pile with a collar at bed level in clear-water current. *Ocean Eng.* **2025**, *320*, 120319. [CrossRef]
20. Zhang, Q.; Tang, G.; Lu, L.; Yang, F. Scour protections of collar around a monopile foundation in steady current. *Appl. Ocean Res.* **2021**, *112*, 102718. [CrossRef]
21. Sumer, B.M.; Fredsøe, J.; Christiansen, N.; Hansen, S.B. Bed Shear Stress and Scour Around Coastal Structures. In *Coastal Engineering 1994*; Proceedings; ASCE Labrary: Reston, VA, USA, 2015; pp. 1595–1609.
22. Mehrzad, R.; Hakimzadeh, H. Experimental Investigation of the Effects of Slotted Cone-Shaped Piers on Scour Reduction Due to Steady Flows. *Int. J. Offshore Polar Eng.* **2017**, *27*, 318–325. [CrossRef]
23. Aghaee-Shalmani, Y.; Hakimzadeh, H. Experimental investigation of scour around semi-conical piers under steady current action. *Eur. J. Environ. Civ. Eng.* **2015**, *19*, 717–732. [CrossRef]
24. Chiew, Y.-M. Mechanics of local scour around submarine pipelines. *J. Hydraul. Eng.* **1990**, *116*, 515–529. [CrossRef]
25. Galán, Á.; González, J. Effects of shape, inlet blockage and wing walls on local scour at the outlet of non-submerged culverts: Undermining of the embankment. *Environ. Earth Sci.* **2019**, *79*, 25. [CrossRef]
26. Lancaster, O.; Cossu, R.; Baldock, T.E. Experimental investigation into 3D scour processes around a gravity based Oscillating Water Column Wave Energy Converter. *Coast. Eng.* **2020**, *161*, 103754. [CrossRef]
27. Qu, L.; An, H.; Draper, S.; Watson, P.; Cheng, L. An experimental investigation of local scour at squat, shallowly embedded subsea structures. *Coast. Eng.* **2025**, *202*, 104851. [CrossRef]
28. Raudkivi, A.J.; Ettema, R. Effect of sediment gradation on clear water scour. *J. Hydraul. Div.* **1977**, *103*, 1209–1213. [CrossRef]
29. Soulsby, R.L.; Whitehouse, R.J. Threshold of sediment motion in coastal environments. In *Pacific Coasts and Ports' 97: Proceedings of the 13th Australasian Coastal and Ocean Engineering Conference and the 6th Australasian Port and Harbour Conference*; Centre for Advanced Engineering, University of Canterbury: Christchurch, New Zealand, 1997; Volume 1, pp. 145–150.
30. Qin, J.; Yang, X.; Wei, K.; Qiu, F. Cross-sectional blockage effect on the drag force of a scaled round-ended pier model under directional flow. *Ocean Eng.* **2022**, *264*, 112532. [CrossRef]
31. Qiu, F.; Wei, K.; Xiang, Q.; Jiang, Z. Effects of local scour and caisson geometry on the drag force of bridge foundations under steady flow. *Appl. Ocean Res.* **2023**, *133*, 103506. [CrossRef]
32. Zhu, Y.; Li, Y.; Xie, L. Hydrodynamic Effects and Scour Protection of a Geotextile Mattress with a Floating Plate. *J. Mar. Sci. Eng.* **2025**, *13*, 2215. [CrossRef]
33. Mohapatra, S.C.; Islam, H.; Guedes Soares, C. Boussinesq Model and CFD Simulations of Non-Linear Wave Diffraction by a Floating Vertical Cylinder. *J. Mar. Sci. Eng.* **2020**, *8*, 575. [CrossRef]
34. Guo, Y.C.; Mohapatra, S.C.; Guedes Soares, C. Experimental study on the performance of an array of vertical flexible porous membrane type breakwater under regular waves. *Ocean Eng.* **2022**, *264*, 112328. [CrossRef]
35. Yakhot, V.; Smith, L.M. The renormalization group, the ϵ-expansion and derivation of turbulence models. *J. Sci. Comput.* **1992**, *7*, 35–61. [CrossRef]
36. Wong, M.; Parker, G. Reanalysis and correction of bed-load relation of Meyer-Peter and Müller using their own database. *J. Hydraul. Eng.* **2006**, *132*, 1159–1168. [CrossRef]
37. Deng, X.; He, S.; Cao, Z. Numerical investigation of the local scour around a coconut tree root foundation under wave-current joint actions. *Ocean Eng.* **2022**, *245*, 110563. [CrossRef]
38. Roulund, A.; Sumer, B.M.; Fredsøe, J.; Michelsen, J. Numerical and experimental investigation of flow and scour around a circular pile. *J. Fluid Mech.* **2005**, *534*, 351–401. [CrossRef]
39. Qu, L.; Draper, S.; An, H.; Watson, P.; Cheng, L.; Harris, J.M.; Whitehouse, R.J.S. Prediction of Scour Around Subsea Shallow Foundations Under Time-Varying Currents. In Proceedings of the ASME 2024 43rd International Conference on Ocean, Offshore and Arctic Engineering, Singapore, 9–14 June 2024.

40. Baykal, C.; Sumer, B.M.; Fuhrman, D.R.; Jacobsen, N.G.; Fredsøe, J. Numerical investigation of flow and scour around a vertical circular cylinder. *Philos. Trans. R. Soc. A Math. Phys. Eng. Sci.* **2015**, *373*, 20140104. [CrossRef] [PubMed]
41. Chang, W.-Y.; Constantinescu, G.; Tsai, W.-F. Effect of array submergence on flow and coherent structures through and around a circular array of rigid vertical cylinders. *Phys. Fluids* **2020**, *32*, 035110. [CrossRef]

Disclaimer/Publisher's Note: The statements, opinions and data contained in all publications are solely those of the individual author(s) and contributor(s) and not of MDPI and/or the editor(s). MDPI and/or the editor(s) disclaim responsibility for any injury to people or property resulting from any ideas, methods, instructions or products referred to in the content.